# Measurements of $ep \to e'\pi^+\pi^-p'$ Cross Sections with CLAS at 1.40 GeV $< W <$ 2.0 GeV and 2.0 GeV$^2 < Q^2 <$ 5.0 GeV$^2$

E.L. Isupov,[2] V.D. Burkert,[1] K. Hicks,[3] B.S. Ishkhanov,[2] V.I. Mokeev,[1] and CLAS Collaboration

[1] *Thomas Jefferson National Accelerator Facility, Newport News, Virginia 23606*

[2] *Skobeltsyn Nuclear Physics Institute and Physics Department at Moscow State University, 119899 Moscow, Russia*

[3] *Ohio University, Athens, Ohio 45701*

(Dated: February 16, 2017)

This paper reports new exclusive cross sections on $ep \to e'\pi^+\pi^-p$ using the CLAS detector at Jefferson Laboratory. These results are presented for the first time at photon virtualities $2.0 < Q^2 < 5.0$ GeV$^2$ in the center-of-mass energy range 1.40 GeV $< W <$ 2.0 GeV, which covers a large part of the nucleon resonance region. The data extend considerably the kinematic reach of previous measurements. Exclusive $ep \to e'\pi^+\pi^-p$ cross section measurements are of particular importance for the extraction of resonance electrocouplings in the mass range above 1.6 GeV.

PACS numbers: 11.55.Fv, 13.40.Gp, 13.60.Le, 14.20.Gk

## I. INTRODUCTION

An extensive research program aimed at the exploration of the structure of excited nucleon states is in progress at Jefferson Lab, employing exclusive meson electroproduction off protons in the nucleon resonance ($N^*$) region. It is an important direction in a broad effort to analyze data from the CLAS detector [1–3].

Studies of exclusive $\pi^+\pi^-p$ electroproduction are of particular importance for the extraction of the $N^*$ electrocoupling amplitudes off protons, for all prominent resonances in the mass range up to 2.0 GeV and at photon virtualities $Q^2 < 5.0$ GeV$^2$.

Many nucleon states in the mass range above 1.6 GeV are known to couple strongly to $N\pi\pi$. The $p\pi^+\pi^-$ final state is therefore a major source of the information on internal structure of these states.

The $\gamma_{r,v}pN^*$ electrocouplings are the primary source of information on many facets of non-perturbative strong interactions, particularly in the generation of the excited proton states from quarks and gluons. Analysis of the $\gamma_v pN^*$ electrocouplings extracted from the CLAS have already revealed distinctive differences in the electrocouplings of states with different underlying quark structures, *e.g.* orbital versus radial quark excitations [1–3].

Furthermore, excited nucleon structure represents a complex interplay between the inner core of three dressed quarks and external meson-baryon cloud [1, 4–6], with their relative contributions evolving with photon virtuality. Therefore, measurements of $\gamma_v pN^*$ electrocouplings allow for a detailed charting of the spatial structure of the nucleon resonances in terms of the quark core and its higher Fock states. Studies of many prominent resonances are needed in order to explore the full complexity of non-perturbative strong interactions in the generation of different excited states. It is through such information that models built on ingredients from QCD are to be confronted, and lead to new insights into the strong interaction dynamics, as well as developments of new theoretical approaches to solve QCD in these cases.

The unique interaction of experiment and theory was recently demonstrated on the quark distribution amplitudes (DA) for the $N(1535)1/2^-$ resonance (a chiral partner of the nucleon ground state). The DA's have become available from Lattice QCD [7], constrained by the CLAS results on the transition $N \to N(1535)1/2^-$ form factor [8], by employing DA's from the Light Cone Sum Rules (LCSR) approach [9]. The comparison of quark DA's in the nucleon ground state and in the $N(1535)1/2^-$ resonance demonstrates a pronounced difference, elucidating the manifestation of Dynamical Chiral Symmetry Breaking (DCSB) in the structure of the ground and excited nucleon states.

Recent advances in Dyson-Schwinger Equations (DSE) now make it possible to describe the elastic nucleon and the transition form factors for $N \to \Delta(1232)3/2^+$ and $N \to N(1440)1/2^+$ starting from the QCD Lagrangian [10, 11]. Currently, DSE relate the $\gamma_v pN^*$ electrocouplings to the quark mass function at distance scales where the quark core is the biggest contributor to the $N^*$ structure, at $Q^2 > 2.0$ GeV$^2$. This success demonstrates the relevance of dressed constituent quarks as effective degrees of freedom in the structure of the ground and excited nucleon states, and emphasizes the need for data on the $Q^2$-dependence of the $\gamma_v pN^*$ electrocouplings to provide access to the momentum dependence of the dressed quark mass.

This provides new insight into one of the still open problems of the Standard Model, that is the nature of hadron mass and the emergence of quark-gluon confinement from QCD [12–14].

The CLAS collaboration has provided much of the world data on meson electroproduction in the resonance excitation region. Nucleon resonance electrocouplings have been obtained from the exclusive channels: $\pi^+n$ and $\pi^0p$ at $Q^2 < 5.0$ GeV$^2$ in the mass range up to 1.7 GeV, $\eta p$ at $Q^2 < 4.0$ GeV$^2$ in the mass range up to 1.6 GeV, and $\pi^+\pi^-p$ at $Q^2 < 1.5$ GeV$^2$ in the mass range up to 1.8 GeV [1, 4, 8, 15–19]. The studies of the $N(1440)1/2^+$ and $N(1520)3/2^-$ resonances with the

CLAS detector [4, 8, 16] have provided most of the information available worldwide on those electrocouplings in the range of photon virtualities 0.25 GeV$^2$ $< Q^2 <$ 5.0 GeV$^2$. The $N(1440)1/2^+$ and $N(1520)3/2^-$ states, together with the $\Delta(1232)3/2^+$ and $N(1535)1/2^-$ resonances [1], are the best understood excited nucleon states to date. Furthermore, results on the $\gamma_v pN^*$ electrocouplings for the high-lying $N(1675)5/2^-$, $N(1680)5/2^+$, and $N(1710)1/2^+$ resonances were determined from the CLAS $\pi^+ n$ data at 1.5 GeV$^2$ $< Q^2 <$ 4.5 GeV$^2$ [15].

Many excited nucleon states with masses above 1.6 GeV decay preferentially to the $N\pi\pi$ final states, making exclusive $\pi^+\pi^- p$ electroproduction off protons a major source of information on these electrocouplings. First accurate results on the electrocouplings of the $\Delta(1620)1/2^-$, which couple strongly to $N\pi\pi$ decay, have been published from the analysis of CLAS data on $\pi^+\pi^- p$ electroproduction off protons [4]. Preliminary results on electrocouplings of two other resonances, the $\Delta(1700)3/2^-$ and the $N(1720)3/2^+$, show a dominance of $N\pi\pi$ decays, which were also obtained from the same channel [17]. Previous studies of these resonances in the $N\pi$ final states suffered from large uncertainties due to small branching fractions for these state decay to N$\pi$.

New analyses of the CLAS $\pi^+\pi^- p$ photo- and electroproduction data [20] combined revealed preliminary evidence for the existence of a $N'(1720)3/2^+$ state. Its spin-parity, mass, total and partial hadronic decay widths, along with the $Q^2$-evolution of the $\gamma_v pN^*$ electrocouplings, have been obtained from a fit to the CLAS data [18]. This is the only candidate state for which information on $\gamma_v pN^*$ electrocouplings have become available, offering access to its internal structure. A successful description of the photo- and electro-production data with $Q^2$-independent mass and hadronic decay widths offers nearly model independent evidence for the existence of this state. Future studies of exclusive $\pi^+\pi^- p$ electroproduction off protons at $W > 1.7$ GeV will also open up the possibility to verify new baryon states observed in a multi-channel global analysis of exclusive photoproduction data by the Bonn-Gatchina group [21].

The resonance electrocouplings from exclusive $\pi^+\pi^- p$ electroproduction off protons are extracted in the ranges of $W <$ 2.0 GeV and $Q^2 <$ 1.5 GeV$^2$ [20, 22]. An extension of the measured $\pi^+\pi^- p$ electroproduction cross sections towards higher photon virtualities is critical for further extraction of resonance electrocouplings at the distance scale where the transition to the dominance of dressed quark degrees of freedom in the $N^*$ structure is expected [1, 2]. These data will provide input for reaction models aimed at determining $\gamma_v pN^*$ electrocouplings for the $N^*$ resonances in the mass range above 1.6 GeV [4, 16, 23]. These data will also provide necessary input for global multi-channel analyses of exclusive meson electro- and hadro-production channels [6, 21, 24–26].

In this paper we present cross sections of $\pi^+\pi^- p$ electroproduction off protons at center of mass energies $\sqrt{s}$ from 1.40 GeV to 2.0 GeV and at photon virtualities $Q^2$ from 2.0 GeV$^2$ to 5.0 GeV$^2$. For the first time, nine independent one-fold differential and fully integrated $\pi^+\pi^- p$ cross sections are determined. As in our previous studies [20, 22], these are obtained by integration of the 5-fold differential cross section over different sets of four kinematics variables. The combined analysis of all nine one-fold differential cross sections gives access to correlations between the one-fold differential cross sections, as they all represent different integrals from the same 5-fold differential cross section.

## II. EXPERIMENTAL DESCRIPTION

The data was collected using the CLAS detector [27] with an electron beam of 5.754 GeV incident on a liquid hydrogen target. The beam current averaged about 7 nA and was produced by the Continuous Electron Beam Accelerator Facility (CEBAF) at the Thomas Jefferson National Accelerator Laboratory (TJNAF). The liquid hydrogen target had a length of 5 cm and was placed 4.0 cm upstream of the center of the CLAS detector. The torus coils of the CLAS detector were run at 3375 A and an additional mini-torus close to the target was run at 6000 A to remove low-energy scattered electrons. The CLAS detector [27] consists of a series of detectors, including three sets of wire drift-chambers (DC) for tracking scattered particles, a Cerenkov detector (CC) to distinguish electrons and pions, an electromagnetic calorimeter (EC) to sample the total energy of particles and a set of time-of-flight scintillators (SC) to record the flight time. For this experiment, the data acquisition trigger was set on the threshold of the CC (at 20 mV pulse height) and a signal in the EC, as explained below. This configuration of the experiment was called the CLAS e1-6 run to distinguish it from other data sets.

### A. Selection of electrons

The particle tracks are determined from the DC coordinates and extrapolated back to the target position. A coordinate system was defined with the z-axis along the beam direction. A histogram of a sampling of electron tracks extrapolated to their point of closest approach to the z-axis is shown in Fig. 1 for one of the six sectors of the CLAS detector. Plots of the other sectors are very similar. A small correction was made for the positioning of the DC in each sector to align the target position. Event selection required a good event to come from the target region.

A scattered electron produces an electromagnetic shower of particles in the EC, and the characteristics of this shower are different for pions and electrons. However, the electromagnetic shower is not fully contained at the edges of the EC, so it is necessary to place an event selection cut to remove unwanted events near the edges. This cut on the fiducial volume is shown in Fig.

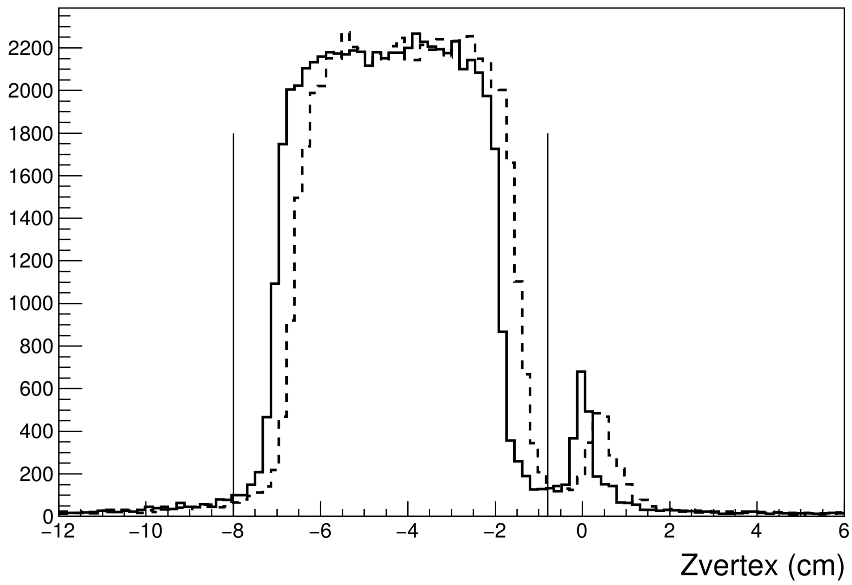


FIG. 1. Vertex reconstruction projected onto the beam axis for sector 2 of CLAS, before (dashed) and after (black) applying corrections to align the sectors of CLAS. The vertical dotted lines show the region of the vertex event selection. The small peak at zero originates from aluminum window 5 cm downstream from the center of the target.

2. The conventional CLAS coordinate system is used for this plot [27]. The edge of the fiducial region is chosen based on many studies of the EC resolution and comparison with known cross sections for elastic e-p scattering.

The EC has two layers, an inner layer (closer to the target) and an outer layer. See Ref. [27] for more details on the EC geometry. The two layers enable separation of charged pions and electrons. Minimum ionizing pions typically lose 26 MeV of energy in the 15 cm of scintillating material of the inner part of the calorimeter, whereas electrons will undergo an electromagnetic shower which deposits more energy ($E_{in}$) in the inner EC layer. A data selection cut $E_{in} > 60$ MeV eliminates most of these pions, as shown in Fig. 3. A more precise selection of electrons comes from the correlation between total energy deposited and momentum. An additional momentum-dependent cut was placed on the ratio of the total energy in the EC and the momentum, $E_{tot}/p$. For a given momentum, the data forms a Gaussian peak for this ratio centered near 0.3. A 2.5-sigma cut on this peak is applied to the data. The loss of events in the Gaussian tail are accounted for by the detector acceptance, where a similar cut is placed on the Monte Carlo simulations.

### B. Particle Identification

Particle identification for hadrons is obtained using the standard method [27] of comparing the particle velocity evaluated from the flight time (from the target to the SC) and from the momentum of a particle track (measured by the DC) for an assumed mass. When the particle mass is correct, the particle's velocity calculated from both methods agree. Fig. 4 top and bottom show the difference between the velocity calculated from the momentum and that from the time-of-flight, which makes a horizontal band at zero velocity difference, for pions and protons, respectively. Below a momentum of about 2 GeV/c, this method provides excellent separation between pions and protons, and reasonable separation up to 2.5 GeV/c.

In the normal current setting of the torus coils of the CLAS detector, positive particles bend outward and negative particles bend inward. In the e1-6 data run, some regions of the CLAS detector were inefficient, due to bad sections of the DC (drift chambers) or a bad SC paddle (time-of-flight scintillators). An example is shown in Fig. 5 for positive pions in sector 3. The inefficient detector regions show up clearly in a plot of the angle of the track at the target, $\theta$, and the measured momentum, $p$. These regions are cut out of both data and Monte Carlo simulation, providing a good match between the real and simulated detector acceptance. In addition, cuts are placed to restrict particle tracks to the fiducial volume of the detector, which eliminates inefficient regions at the edges of the DC detectors. The fiducial cuts are standard for CLAS and are described elsewhere [20].

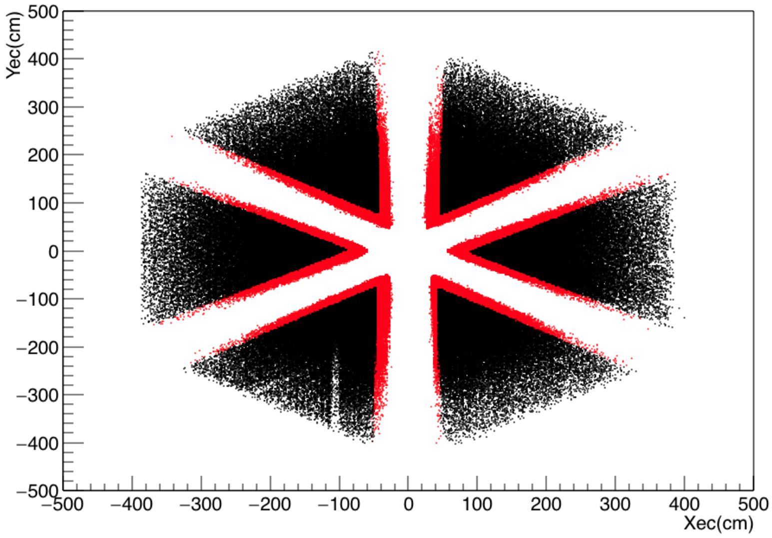


FIG. 2. (Color Online) The position of electron events in the EC for the six sectors of CLAS for all events (light gray or red online) and selected events (black). The stripe seen in the lower left sector is due to inefficient phototubes on a few scintillator strips of the EC. The same inefficiencies are introduced in the simulations of the detector acceptance.

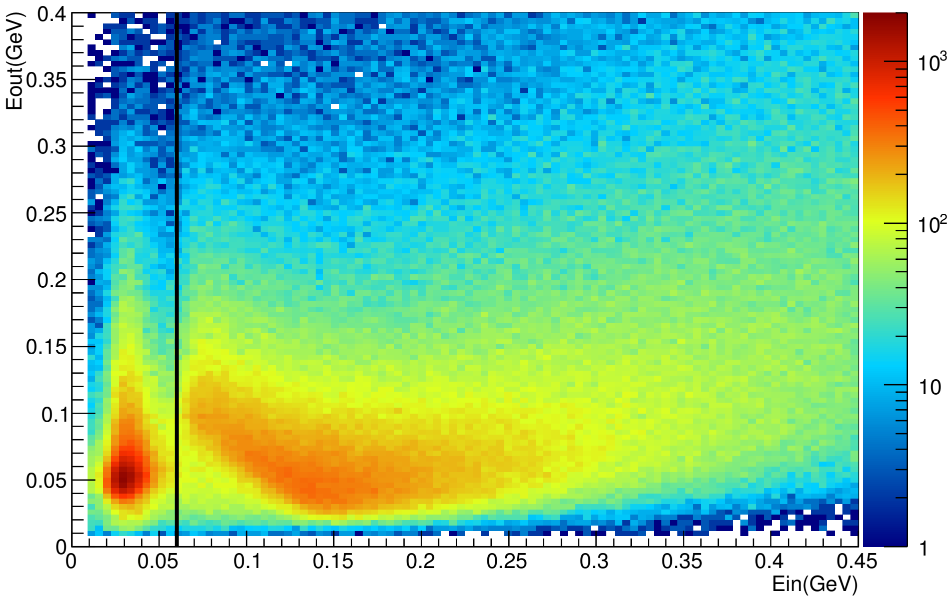


FIG. 3. (Color Online) The energy deposited in the inner ($E_{in}$) and outer ($E_{out}$) layers of the EC for all particles. The line corresponds to 60 MeV, which separates the pions (to the left) and electrons (to the right).

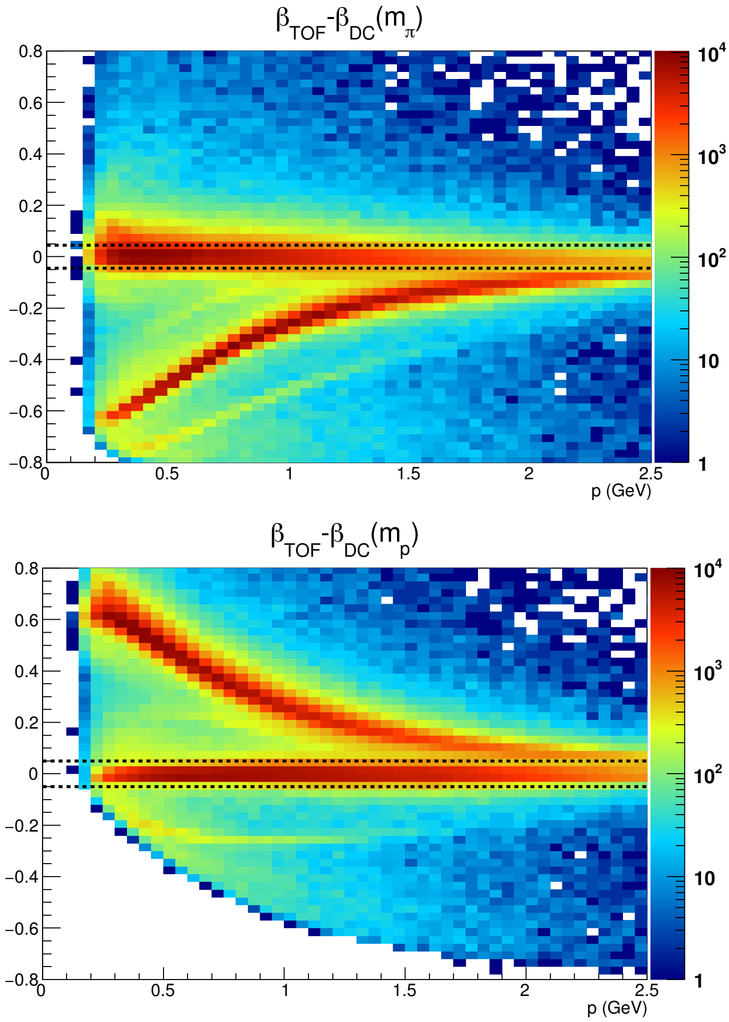


FIG. 4. (Color Online) Velocity difference $\beta_{TOF} - \beta_{DC}$ vs. momentum for pions (top) and protons (bottom).

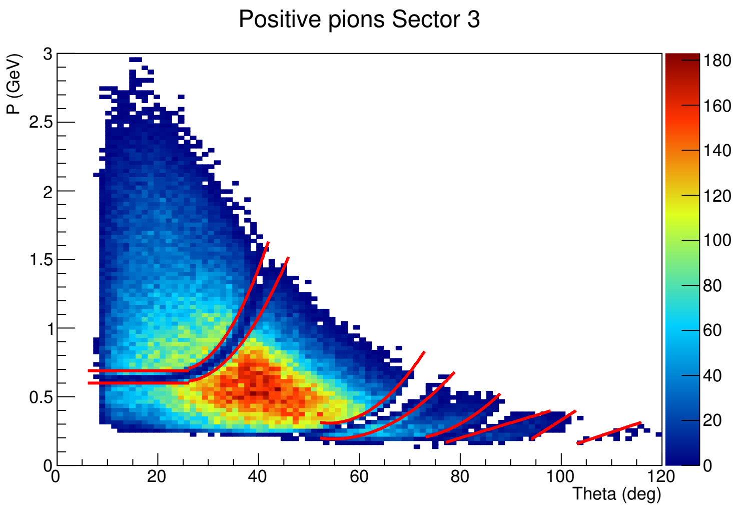


FIG. 5. (Color Online) Histogram of the correlation between initial angle, Theta ($\theta$), and momentum, $p$, for tracks of positive pions in sector 3 of CLAS. Inefficient regions of the detector are removed, shown by the solid lines.

### C. Event Selection

Events with a detected electron, proton and positive pion were retained for further analysis. The reaction of interest here is $ep \rightarrow e'p'\pi^+\pi^-$, where the primed quantities are for the final state. The negative pion is bent toward the beamline and may bend outside of the detector acceptance. Instead, we reconstruct the mass of the pion using the missing mass technique. The missing mass squared for these events is shown in Fig. 6, with a clean peak at the pion mass. The peak position and width compare very well with Monte Carlo (MC) simulated events. The larger number of events in the data at higher missing mass are due to radiative events, where the electron radiates a low-energy photon either just before or just after it scatters from the proton. The loss of these events from the peak can be calculated using standard methods (described later) and are corrected for in the final analysis. After all selections have been applied, there remain 336 668 exclusive $p\pi^+\pi^-$ events. The distribution of data events for this measurement are shown in Fig. 7 as a function of the center of mass (CM) energy, $W$, and the four-momentum transfer to the virtual photon, $Q^2$. The data were binned, as shown by the black lines in the plot, to get the fully integrated cross section dependence on the $W$ and $Q^2$.

### D. Reaction Kinematics

The kinematics of the reaction are shown in Fig. 8. The scattered electron defines a plane, which in our coordinate system is the x-z plane. The direction of the z-axis is chosen to align with the virtual photon momentum vector. The y-axis is normal to the scattering plane with its direction given as shown in Fig. 8. The virtual photon and the outgoing $\pi^-$ form another plane, labeled A in Fig. 8, with angles $\theta$ and $\phi$ as shown. We also need angles for the $\pi^+$ and the final protons $p'$, as described next.

A plane is defined by the outgoing particles $\pi^+$ and $p'$, labeled B in Fig. 8, which intersects with plane A. Note that in the CM frame, the three-momenta of all three final hadrons are located in the common plane B. The angle between the A and B planes is given by $\alpha_{[\pi^-p][\pi^+p']}$ as shown in Fig. 8. In order to calculate this angle, unit vectors $\beta$, $\gamma$ and $\delta$ are defined as shown in Fig. 8. We evaluated these unit vectors as given in Ref. [22]. Using the three CM angles defined here, along with the invariant masses of the final $\pi^-\pi^+$ and $\pi^+p'$ hadron pairs $M_{\pi^-\pi^+}$ and $M_{\pi^+p}$, gives a complete description of the reaction kinematics.

The 3-body final state is unambiguously determined by 5 kinematics variables. Indeed, 3 final particles could be described by $4 \times 3 = 12$ components of their 4-momenta. All these particles are on-shell. So, it gives us 3 restrictions $E_i^2 - P_i^2 = m_i^2$ $(i = 1, 2, 3)$. Energy-momentum conservation imposes 4 additional constraints for the final particles, so that there are 5 remaining kinematics variables which determine unambiguously the 3-body final state kinematics. In the electron scattering process $ep \rightarrow ep'\pi^+\pi^-$ we also have variables $W$, $Q^2$ that fully define the initial state kinematics for a given energy of the incoming electrons. So the electron scattering cross sections for double charged pion production should be 7-fold differential: 5 variables for the final hadrons plus $W$ and $Q^2$ determined by electron scattering kinematics. Such 7-fold differential cross sections may be written as $\frac{d^7\sigma}{dW dQ^2 d^5\tau}$, where $d^5\tau$ is 5-fold phase space for the final hadron kinematics.

Three sets of five variables were used. The five variables with respect to the $\pi^-$ CM angle $(M_{\pi^+\pi^-}, M_{\pi^+p}, \theta_{\pi^-}, \varphi_{\pi^-}, \alpha_{[\pi^-p][\pi^+p']})$ were calculated from 3-momenta of the final particles $\vec{P}_{\pi^-}$, $\vec{P}_{\pi^+}$, $\vec{P}_{p'}$. Two other sets with respect to the $\pi^+$ and $p'$ CM angles were obtained by cyclic permutation of the aforementioned variables of the first set. All 3-momenta used below, if not specified otherwise, are defined in the CM frame.

The $M_{\pi^+\pi^-}$, $M_{\pi^+p}$ invariant masses are related to four momenta of the final particles as:

$$M_{\pi^+\pi^-} = \sqrt{(P_{\pi^+} + P_{\pi^-})^2}$$
$$M_{\pi^+p'} = \sqrt{(P_{\pi^+} + P_{p'})^2} \quad (1)$$
$$(2)$$

where $P_i$ stand for the final particle four-momentum.

The angle $\theta_{\pi^-}$ between 3-momentum of the initial photon and final $\pi^-$ in the CM frame is calculated as:

$$\theta_{\pi^-} = \cos^{-1}\left(\frac{(\vec{P}_{\pi^-}\vec{P}_{\gamma})}{|\vec{P}_{\pi^-}||\vec{P}_{\gamma}|}\right) \quad (3)$$

The $\varphi_{\pi^-}$ angle is defined as:

$$\varphi_{\pi^-} = \tan^{-1}\left(\frac{P_{y\pi^-}}{P_{x\pi^-}}\right); \;\; P_{x\pi^-} > 0; P_{y\pi^-} > 0 \quad (4)$$
$$\varphi_{\pi^-} = \tan^{-1}\left(\frac{P_{y\pi^-}}{P_{x\pi^-}}\right) + 2\pi; \;\; P_{x\pi^-} > 0; P_{y\pi^-} < 0 \quad (5)$$
$$\varphi_{\pi^-} = \tan^{-1}\left(\frac{P_{y\pi^-}}{P_{x\pi^-}}\right) + \pi; \;\; P_{x\pi^-} < 0; P_{y\pi^-} < 0 \quad (6)$$
$$\varphi_{\pi^-} = \tan^{-1}\left(\frac{P_{y\pi^-}}{P_{x\pi^-}}\right) + \pi; \;\; P_{x\pi^-} < 0; P_{y\pi^-} > 0 \quad (7)$$
$$\varphi_{\pi^-} = \pi/2; \;\; P_{x\pi^-} = 0; P_{y\pi^-} > 0 \quad (8)$$
$$\varphi_{\pi^-} = 3\pi/2; \;\; P_{x\pi^-} = 0; P_{y\pi^-} < 0 \quad (9)$$

The calculation of the angle $\alpha_{[\pi^-p][\pi^+p']}$ , between the planes A and B is more complicated. First we determine two auxiliary vectors $\vec{\gamma}$ and $\vec{\beta}$. The vector $\vec{\gamma}$ is a unit vector perpendicular to the 3-momentum $\vec{P}_{\pi^-}$, directed outward and situated in the plane given by the virtual photon 3-momentum and 3-momentum $\vec{P}_{\pi^-}$. The vector $\vec{\beta}$ is a unit vector perpendicular to the 3-momentum of

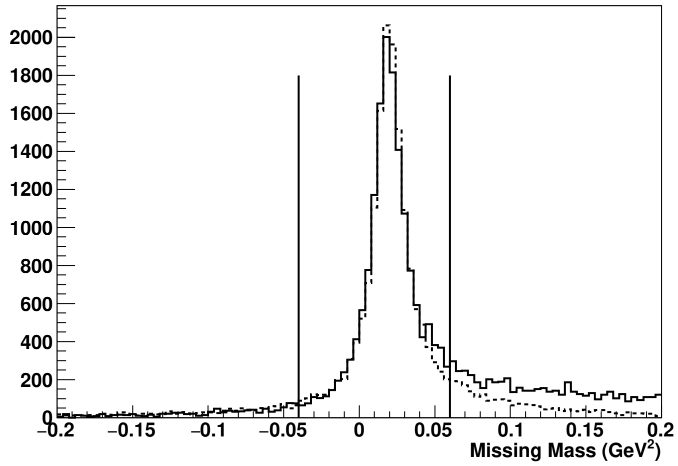


FIG. 6. Square of the missing mass, showing a peak at the pion mass squared. Dashed curve is MC, solid curve is DATA. The vertical lines show the applied cut.

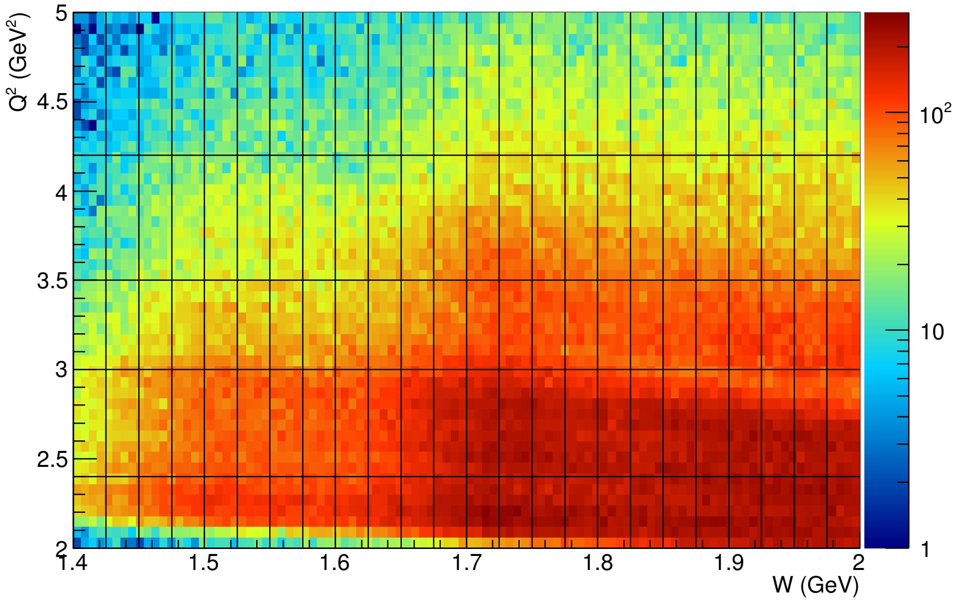


FIG. 7. (Color Online) The kinematic coverage of the data, shown as a scatterplot of events as a function of center of mass energy $W$ and 4-momentum transfer, $Q^2$. Bins are shown within which the integrated and nine one-fold differential $\pi^+\pi^-p$ cross sections were obtained.

the $\pi^-$, directed toward the 3-momentum $\vec{P}_{\pi^+}$ and situated in the plane composed by the $\pi^+$ and $p'$ 3-momenta. As mentioned above, the 3-momenta of $\pi^+$, $\pi^-$ and $p'$ are in the same plane, since in the CM frame their total 3-momentum should be equal to zero. Then the angle between two planes is,

$$\alpha_{[\pi^-p][\pi^+p']} = \cos^{-1}(\vec{\gamma} \cdot \vec{\beta}) \tag{10}$$

where the inverse cosine function runs between zero and $\pi$. On the other hand, the angle between the planes A and B may vary between zero and $2\pi$. To determine the angle $\alpha_{[\pi^-p][\pi^+p']}$ in a range between $\pi$ and $2\pi$ we look at the relative direction of the vector $\vec{P}_{\pi^-}$ and vector product $\vec{\delta}$ from the unit vectors $\vec{\gamma}$ and $\vec{\beta}$:

$$\vec{\delta} = \vec{\gamma} \times \vec{\beta} \tag{11}$$

If the vector $\vec{\delta}$ is collinear to $\vec{P}_{\pi^-}$, the $\alpha_{[\pi^-p][\pi^+p']}$ angle

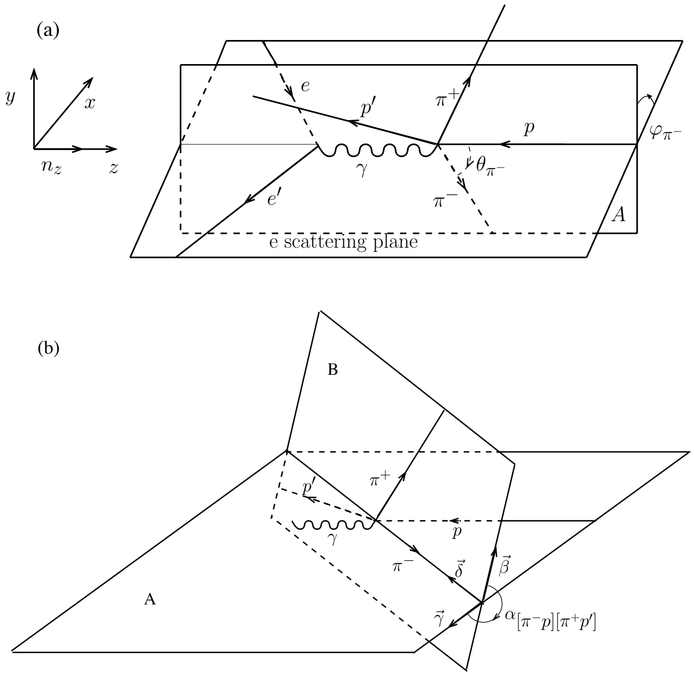


FIG. 8. Angular variables from the set of 5 variables defined by Eq 14 for the description of $ep \to e'p'\pi^+\pi^-$ reaction in the CM frame of the final-state hadrons. Panel (a) shows the $\pi^-$ spherical angles $\theta_{\pi^-}$ and $\varphi_{\pi^-}$. Plane C represents the electron scattering plane. Plane A is defined by the 3-momenta of the initial state proton and the final state $\pi^-$. Panel (b) shows the angle $\alpha_{[\pi^-p][\pi^+p']}$ between the two defined hadronic planes A and B. Plane B is defined by the 3-momenta of the final state $\pi^+$ and $p'$. The unit vectors $\vec{\gamma}$ and $\vec{\beta}$ are normal to the $\pi^-$ three-momentum in the planes A and B, respectively.

is determined from Eq. (10). In the case of anti collinear vectors $\vec{\delta}$ and $\vec{P}_{\pi^-}$:

$$\alpha_{[\pi^-p][\pi^+p']} = 2\pi - \cos^{-1}(\vec{\gamma}\cdot\vec{\beta}) \tag{12}$$

The vectors $\vec{\gamma}$, $\vec{\beta}$, and $\vec{\delta}$ may be expressed in terms of the final hadron 3-momenta as given in Ref. [22].

### E. Cross section formulation

The 7-fold differential cross section may be written as: $\frac{d^7\sigma}{dWdQ^2dM_{\pi^+p}dM_{\pi^+\pi^-}d\Omega_{\pi^-}d\alpha_{[\pi^-p][[\pi^+p']}}$. These cross sections were calculated from the quantity of selected events collected in the respective 7-differential cell as:

$$\left(\frac{\Delta N}{eff\cdot R}\right)\left(\frac{1}{\Delta W\Delta Q^2\Delta\tau_{\pi^-}L}\right) \tag{13}$$

where $\Delta N$ are the numbers of events inside the 7-dimensional bin, $eff$ is the efficiency for the $\pi^+\pi^-p$ event detection in the 7-dimensional bin, $R$ is the radiative correction factor (described in section II G), $L$ is the integrated luminosity (in units of $\mu b^{-2}$), $\Delta W$ and $\Delta Q^2$ are determined by binning in the electron scattering kinematics, and $\Delta\tau_{\pi^-}$ is binned from the hadronic 7-dimensional phase space:

$$\Delta\tau_{\pi^-} = \Delta M_{\pi^+p}\Delta M_{\pi^+\pi^-}\Delta\cos(\theta_{\pi^-})\Delta\varphi_{\pi^-}\Delta\alpha_{[\pi^-p][\pi^+p']}\,. \tag{14}$$

In the single photon exchange approximation, the electron scattering cross section is related to the hadronic cross section as:

$$\frac{d\sigma}{dM_{p\pi^+}dM_{\pi^+\pi^-}d\Omega_{\pi^-}d\alpha_{[\pi^-p][\pi^+p']}} = \frac{1}{\Gamma_v}\frac{d\sigma}{dWdQ^2dM_{p\pi^+}dM_{\pi^+\pi^-}d\Omega_{\pi^-}d\alpha_{[\pi-p][\pi^+p']}}$$

where $\Gamma_v$ is the virtual photon flux, given by

$$\Gamma_v = \frac{\alpha}{4\pi}\frac{1}{E_{beam}^2M_p^2}\frac{W(W^2-M_p^2)}{(1-\varepsilon)Q^2} \tag{15}$$

where $\alpha$ is the fine structure constant, $M_p$ is the proton mass and $\varepsilon$ is the virtual photon transverse polarization,

$$\varepsilon = \left(1+2\left(1+\frac{\omega^2}{Q^2}\right)\tan^2\left(\frac{\theta_e}{2}\right)\right)^{-1} \tag{16}$$

where $\omega = E_{beam} - E_{e'}$, $\theta_e$ is the electron scattering angle in the lab frame and $W$, $Q^2$ and $\theta_e$ are evaluated at the center of the bin. The 7-dimensional phase space for exclusive $ep \to e^{'}\pi^+\pi^-p^{'}$ electroproduction covered in our data set consists of 4 320 000 cells. Because of the correlation between $\pi^+\pi^-$ and $\pi^+p$ invariant masses of the final hadrons imposed by the energy-momentum conservation, only 3 606 120 7-d cells are kinematically allowed. They are populated by just 336 668 selected exclusive charged double pion electroproduction off protons events. Most of 7-d cells are either empty or contain just one measured event. It makes virtually impossible to evaluate the 7-fold differential electron scattering or 5-fold differential virtual photon cross sections from our data. Following previous studies [16, 20, 22], in order to achieve sufficient accuracy of these data, the 5-fold differential cross sections were integrated over different sets of four variables, producing independent 1-fold differential cross sections. The first step of physics analysis, aimed at determining the contributing reaction mechanisms, it is even more beneficial to use the integrated single differential cross-sections, since the structures and steep evolution of these cross-sections elucidate the role of effective meson-baryon diagrams. So in practice, we analyzed sets of single differential cross sections obtained by integration of the 5-differential cross sections over 4 variables in each bin of $W$ and $Q^2$. We used the following set of four one-fold differential cross sections using $d^5\tau_{\pi^-}$

as defined by Eq. (14):

$$
\begin{aligned}
\frac{d\sigma}{dM_{\pi^+\pi^-}} &= \int \frac{d^5\sigma}{d^5\tau_{\pi^-}} dM_{\pi^+p} d\Omega_{\pi^-} d\alpha_{[\pi^-p][\pi^+p']} \\
\frac{d\sigma}{dM_{\pi^+p}} &= \int \frac{d^5\sigma}{d^5\tau_{\pi^-}} dM_{\pi^+\pi^-} d\Omega_{\pi^-} d\alpha_{[\pi^-p][\pi^+p']} \\
\frac{d\sigma}{d(-cos(\theta_{\pi^-}))} &= 2\pi \int \frac{d^5\sigma}{d^5\tau_{\pi^-}} dM_{\pi^+\pi^-} dM_{\pi^+p} d\alpha_{[\pi^-p][\pi^+p']} \\
\frac{d\sigma}{d\alpha_{[\pi^-p][\pi^+p']}} &= \int \frac{d^5\sigma}{d^5\tau_{\pi^-}} dM_{\pi^+\pi^-} dM_{\pi^+p} d\Omega_{\pi^-} \ .
\end{aligned} \tag{17}
$$

Five other one-fold differential cross sections were obtained by integration of the 5-fold differential cross sections binned over the $\pi^+$ and proton kinematics, using $d^5\tau_{\pi^+}$ and $d^5\tau_{p'}$ defined similarly to Eq. (14):

$$
\begin{aligned}
\frac{d\sigma}{d(-cos(\theta_{\pi^+}))} &= 2\pi \int \frac{d^5\sigma}{d^5\tau_{\pi^+}} dM_{p'\pi^-} dM_{\pi^+p} d\alpha_{[p'\pi^-][p\pi^+]} \\
\frac{d\sigma}{d\alpha_{[p'\pi^-][p\pi^+]}} &= \int \frac{d^5\sigma}{d^5\tau_{\pi^+}} dM_{p'\pi^-} dM_{\pi^+p} d\Omega_{\pi^+} \\
\frac{d\sigma}{dM_{\pi^-p'}} &= \int \frac{d^5\sigma}{d^5\tau_{\pi^+}} dM_{p'\pi^+} d\Omega_{\pi^+} d\alpha_{[p'\pi^-][p\pi^+]}, \\
\frac{d\sigma}{d(-cos(\theta_{p'}))} &= 2\pi \int \frac{d^5\sigma}{d^5\tau_{p'}} dM_{\pi^+\pi^-} dM_{\pi^-p'} d\alpha_{[\pi^+\pi^-][p'p]} \\
\frac{d\sigma}{d\alpha_{[\pi^+\pi^-][p'p]}} &= \int \frac{d^5\sigma}{d^5\tau_{p'}} dM_{\pi^+\pi^-} dM_{\pi^-p'} d\Omega_{p'} \ .
\end{aligned} \tag{18}
$$

The statistic uncertainties for 1-fold differential cross sections obtained from our data are in the range from 14 % at smallest photon virtuality ($Q^2$=2.1 GeV$^2$) to 20 % at biggest photon virtuality ($Q^2$=4.6 GeV$^2$), which are comparable with achieved in our previous data [20, 22] from which resonance electrocouplings were successfully extracted [4, 16].

### F. Detector Simulations and Efficiencies

A Monte Carlo event generator was similar to that described in Ref. [20]. This event generator is capable to simulate the event distribution for major meson photo- and electro-production channels in the N* excitation region. The input to the event generator includes various kinematical parameters($W$, $Q^2$, electron angles and so on) along with a description of the hydrogen target geometry. This event generator also generates radiative effects, calculated according to [28]. Simulation of $\pi^+\pi^-p$ electroproduction off protons events was based on the old version of the Jlab-MSU model JM06 [29–31], adjusted to reproduce the measured event kinematic distributions. The generated events are fed into the standard CLAS detector simulation software, based on CERN's Geant package, called GSIM. The detector efficiency for a given 7-fold kinematic bin is then given by

$$eff = \frac{N_{rec}}{N_{gen}} \tag{19}$$

where $N_{gen}$ is the number of events generated for a given kinematic bin, and $N_{rec}$ is the number of events reconstructed by the GSIM software. The same detector fiducial area was used for both data and simulations to restrict the reconstructed tracks to the regions of the CLAS detector where efficiency evaluations are reliable. After making the fiducial cuts, this gives us the detector efficiency tables for a given kinematic bin that were used to calculate the cross sections.

In the data analysis for some 7-d cells, we had a reasonable number of generated (simulated) events, but the quantity of accepted events was equal to zero. Such situations represent an indication of zero CLAS detector acceptance in these kinematics regions. We need to account for the contribution of such "blind" area to the integrals for the single differential cross sections given above.

To estimate the contributions to the cross sections from detector blind areas, we used information from the event generator. We evaluated such contributions based on the cross section description of the JM06 event generator. The JM06 model [29–31] was not previously compared with charged double pion electroproduction data at $Q^2$ > 2.0 GeV$^2$. Therefore, the JM06 model was further adjusted to the measured event distributions over the $\pi^+\pi^-p$ final state kinematics variables discussed above. After adjustment, the event generator gives a fair description of the data on the measured event distributions over kinematics variables for all 1-fold differential cross sections. As a representative example, the comparison between measured and simulated event distributions is shown in Fig. 9. A comparable quality of agreement has been achieved over the entire kinematic range covered by our measurements.

To obtain the 5-fold differential virtual photon cross sections in the blind areas $\frac{d^5\sigma}{dM_{p\pi^+}dM_{\pi^+\pi^-}d\Omega_{\pi^-}d\alpha_{[\pi^-p][\pi^+p']}}$ we used as input:

- the number of measured data events (we weigh these events with the integral efficiency inside 5-d bin) in the current $(W, Q^2)$ bin, integrated over all hadronic variables for the $\pi^+\pi^-p$ final state $N_{data,int}$;

- the number of these events estimated from event generator $N_{generated,int}$;

- the number of generated events in a 7-dimensional blind kinematic bin $(W, Q^2, M_{p\pi^+}, \Omega_{\pi^-}, \alpha_{\pi^+,p})$ which we call $N^{7D}_{generated}$.

Using the event generator as a guide, we extrapolated the number of events measured outside of the blind bin into the blind bin. Thus, the number of counts given above for the 5-differential cross sections *in the blind bins only* were calculated as:

$$\Delta N = \frac{N_{data,int}}{N_{generated,int}} N^{7D}_{generated} \tag{20}$$

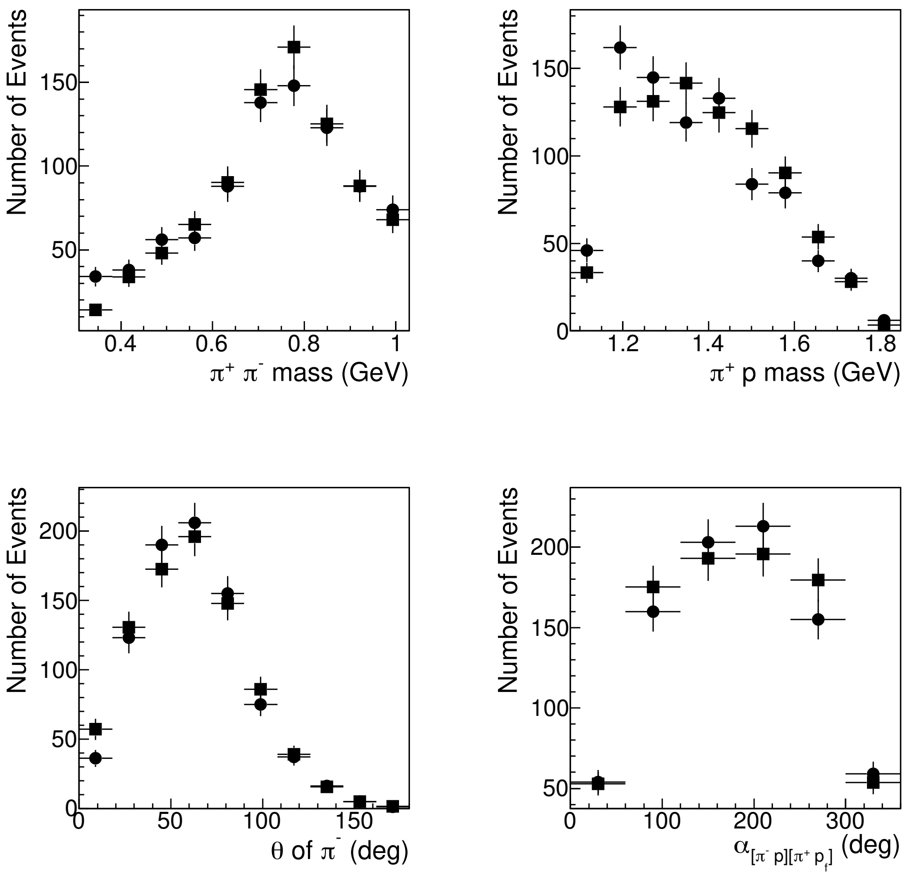


FIG. 9. The comparison between measured event distributions (circles) and simulated event distributions (squares) within the framework of the JM06 model [29–31] further adjusted in order to reproduce the measured event distributions in the bin of $W$=1.99 GeV, $Q^2$=4.6 GeV$^2$

The 5-differential virtual photon cross sections in the blind bins were computed from $\Delta N$ in Eq.(20) according to Eqs (13-16).

The comparison between 1-fold differential cross sections obtained with and without generated events inside the blind bins is shown in Fig. 10. Except for the two bins of maximal CM-$\theta_{\pi^+}$ angles, the difference between the two methods is rather small, and is inside the statistical uncertainties for most points. The estimated uncertainty introduced by this extrapolation method has an upper limit of 5-10%, depending on the kinematics.

### G. Radiative Corrections

To estimate the influence of radiative correction effects, we simulated 2 pion events using the above event generator both with and without radiative effects. For the simulation of radiative effects in double pion electroproduction, the well known Mo and Tsai procedure [28] is used. As described above, we integrate the 5-fold 2 pion cross sections over 4 variables to get 1-fold differential cross-sections. This integration considerably reduces the influence of the final hadron kinematics variables on radiative correction factors for the analyzed single differential cross sections. The radiative correction factor $R$ in the above cross section formula was determined as:

$$R = \frac{N^{2D}_{rad}}{N^{2D}_{norad}} \ , \tag{21}$$

where $N^{2D}_{rad}$ and $N^{2D}_{norad}$ are numbers of generated events in each $(W, Q^2)$ bin with and without radiative effects. We then fit the inverse factor $1/R$ over the $W$ range in each $Q^2$ bin. The factor $1/R$ for the bin $4.2 < Q^2 < 5.0$ is plotted as function of $W$ on Fig. 11. A few words should be said about the behavior of this factor. Since the radiation migrates events from the lower $W$ to higher $W$ and because the structure at $W$ of around 1.7 GeV is the most prominent feature of the cross-sections, there is a small enhancing bump for the factor $1/R$.

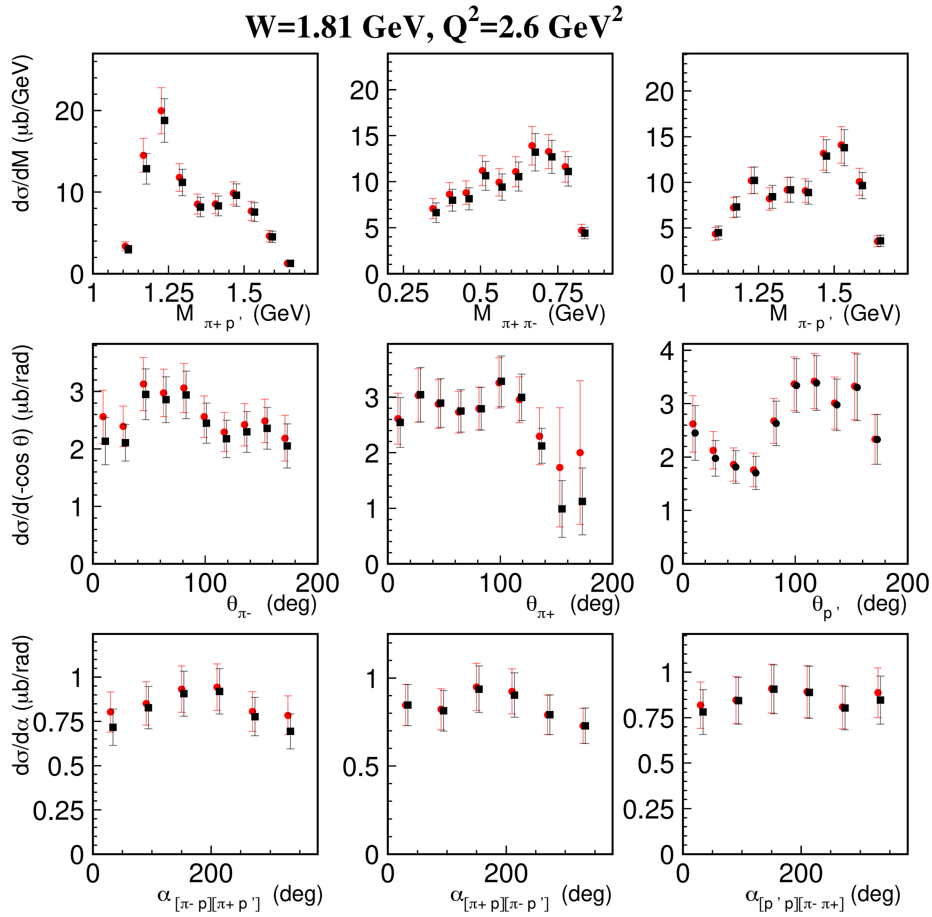


FIG. 10. (color online) Impact of the interpolation of the 5-fold $\pi^+\pi^-p$ differential cross sections into the CLAS blind areas to the nine one-fold differential cross sections at $W$=1.81 GeV and $Q^2$=2.6 GeV$^2$. One-fold differential cross section obtained assuming zero five-fold differential cross sections and the interpolated values for these cross sections in the blind CLAS area are shown by black squares and red circles, respectively.

### H. Systematic Uncertainties

One of the main sources of systematic errors in this experiment is the uncertainty in the luminosity, $L$. This can arise from miscalibration of the Faraday cup, target density instabilities, computer data-acquisition live-time, and other factors. However, the presence of the elastic events in the data set allows us to check the normalization of the cross sections by comparing the elastic cross sections to the world data. This way we can combine the normalization, electron detection, electron tracking and electron identification errors into one global uncertainty factor. In Fig. 12 the ratio of the elastic cross section to the Bosted parametrization [32] is shown. The parametrization cross section are after radiative effects are applied, and the elastic cross sections from the CLAS data are not corrected for radiative effects, so they are directly comparable. One can see most of the points are positioned within the red lines, indicating 10% offsets. This procedure allows us to assign 10% global error due to the luminosity.

We restrict the missing mass to be close to the $\pi^-$ peak in order to select two pion events. This event selection (or 'missing mass 'cut") causes loss of some events. Uncertainties due to such losses were estimated by using Monte Carlo simulations for the acceptance calculations. The error associated with the missing mass cut was estimated by calculating the difference in the cross sections with two different missing mass cut applied both on the real data and Monte-Carlo data sample. The missing mass cut used in the analysis is $-0.04 < M^2_{\pi^- X} < 0.06$ GeV$^2$ so we varied the range of this cut to $-0.02 < M^2_{\pi^- X} <$ 0.03 GeV$^2$ to estimate the systematic uncertainty due to the missing mass cut.

We use the following method for estimating systematic uncertainties. In each case for a given observable (*e.g.*, mass distributions) we can calculate the relative difference $(\sigma-\sigma_c)/\sigma$, where $\sigma_c$ is the recalculated cross-section with a more narrow missing mass cut. We expect to see a gaussian-like distribution for the relative difference distribution. The difference between the center of this distri-

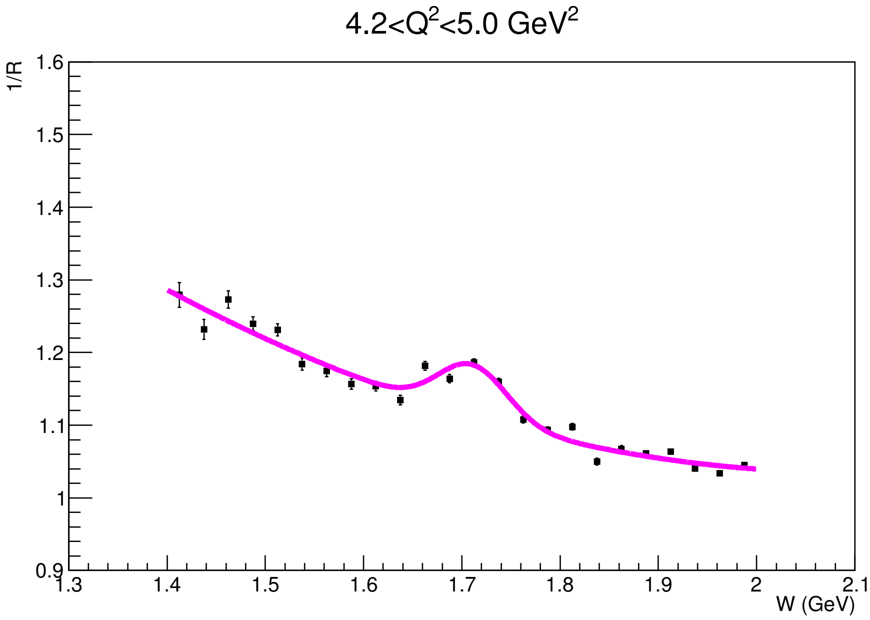


FIG. 11. (Color Online) The radiative corrections factor $1/R$ for the bin $4.2 < Q^2 < 5.0$ GeV$^2$

bution and zero is a measure of systematic uncertainties. From this, we estimated the systematic uncertainty due to the missing mass cuts are about 4.2% of the measured differential cross sections.

To estimate the influence of detector fiducial area cuts, we recalculated cross-sections without applying fiducial cuts to the hadrons. Again, we construct the relative difference $(\sigma - \sigma_c)/\sigma$, where $\sigma_c$ is the recalculated cross-section without hadron fiducial cuts. The result is that we see a systematic decrease of about 2% of the cross-sections.

We also varied the particle identification criteria, which is a cut on the calculated speed and momentum of the detected hadrons. In our analysis we apply $2\sigma$ cut, so to estimate the influence of these cuts to our results we recalculated cross-sections with $3\sigma$ cut. By widening the particle identification cuts and using the same relative difference procedure as above, we see systematic increase of about 4.6% of the cross-sections.

Adding in quadrature the various systematic uncertainties, which are dominated by the luminosity, we find an overall (global) systematic uncertainty of 14% for the cross sections reported here. The summary of systematic uncertainties can be found in the Table I. In addition, there are additional point-to-point uncertainties, dependent on the 5-dimensional kinematics, due to the extrapolation procedure to fill blind bins. This systematic uncertainty for the 1-fold differential cross sections is estimated (from the differences shown in Fig. 10) to range from 5-10% as an upper limit, but may be smaller in regions where the JM06 model gives a good representation of the measured cross sections.

| Sources of systematics | uncertainty, % |
|---|---|
| Electron ID and luminosity | 10 |
| Missing mass cut | 4.2 |
| Hadron fiducial cuts | 2 |
| Hadron ID cuts | 4.6 |
| Radiative corrections | 5 |
| Event Generator | 5 |
| Total | 14 |

TABLE I. Summary of sources of systematic uncertainties

## III. RESULTS AND DISCUSSION

The fully integrated $\pi^+\pi^-p$ electroproduction cross sections obtained by integration of the 5-fold differential cross sections are shown in Fig. 13 for five $Q^2$-bins. Two structures located at $W$ 1.5 GeV and 1.7 GeV produced by the resonances of the second and third resonance regions are the major features in $W$-evolution of the integrated cross sections observed in the entire range of $Q^2$ covered by the CLAS measurements.

The results on $\pi^+\pi^-p$ electroproduction cross sections discussed in section II open up the possibility to extend our knowledge of the $\gamma_v pN^*$ electrocouplings of many resonances up to photon virtualities up to $Q^2 = 5$ GeV$^2$, in particular for the states in the mass range above 1.6 GeV [4, 18]. This $Q^2$ range corresponds to the distance scale where the transition to the dominance of quark core contributions to the resonance structure takes place [1, 2, 10, 11].

Here, we discuss the prospects for the extraction of resonance parameters from the new data based on comparisons between the measured nine one-fold differential

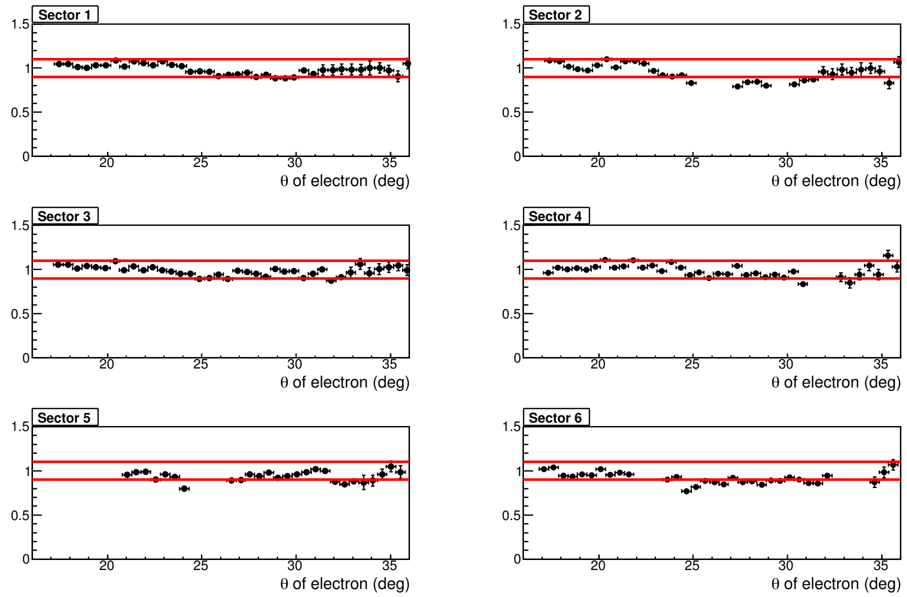


FIG. 12. (Color Online) Ratio of the elastic cross section to the Bosted parametrization. The horizontal lines represent 10% offset.

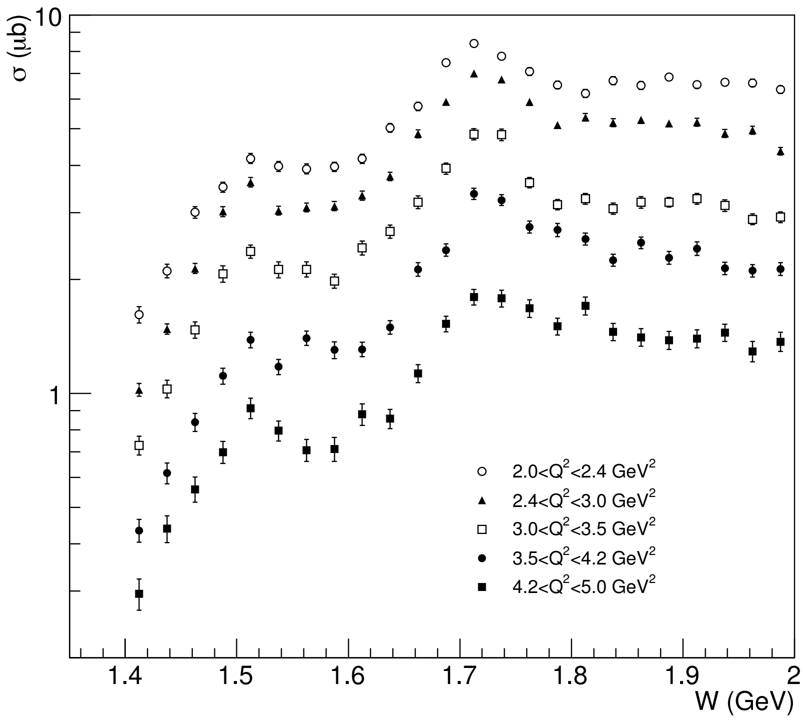


FIG. 13. Fully integrated $\pi^+\pi^-p$ electroproduction off protons cross sections at the photon virtualities $Q^2$=2.2, 2.6, 3.2, 3.8, 4.6 GeV$^2$

cross sections and projected resonant contributions. Resonant contributions are computed within the framework of the recent JM model version [4, 16, 23] employing the unitarized Breit-Wigner ansatz for the resonant amplitudes described in [16] and using interpolation of resonance electrocouplings previously extracted in the analyses of exclusive meson electroproduction data from CLAS [1, 2, 15].

So far, $\gamma_v pN^*$ electrocouplings are available for excited nucleon states in the mass range up to 1.8 GeV/c$^2$. They were obtained from various CLAS data in the exclusive channels: $\pi^+ n$ and $\pi^0 p$ at $Q^2 < 5.0$ GeV$^2$ in the mass range up to 1.7 GeV/c$^2$, $\eta p$ at $Q^2 < 4.0$ GeV$^2$ in the mass range up to 1.6 GeV/c$^2$, and $\pi^+\pi^- p$ at $Q^2 < 1.5$ GeV$^2$ in the mass range up to 1.8 GeV/c$^2$. A summary of the results on resonance $\gamma_v pN^*$ electrocoupling available can be found in the Table II. The $\gamma_v pN^*$ electrocoupling values together with the appropriate references are available from our web-page [33].

The $\gamma_v pN^*$ electrocouplings employed in evaluations of the resonant contribution to the differential $\pi^+\pi^- p$ cross sections here are obtained from interpolation or extrapolation of the experimental results [33] by polynomial functions of $Q^2$. The estimated resonance electrocouplings can be found at [34]. For low-lying excited nucleon states in mass range $M_{N^*} < 1.6$ GeV/c$^2$, the experimental results on $\gamma_v pN^*$ electrocouplings are available at photon virtualities up to 5.0 GeV$^2$. Electrocouplings of these resonances are estimated by interpolating the data points. Electrocouplings of $N(1675)5/2^-$, $N(1680)5/2^+$, and $N(1710)1/2^+$ resonances are available from $\pi^+ n$ electroproduction data [15]. To estimate their contributions to $\pi^+\pi^- p$ electroproduction cross sections, we interpolate those results in $Q^2$.

Electrocouplings of the $\Delta(1620)1/2^-$, $\Delta(1700)3/2^-$, and $N(1720)3/2^+$ resonances are available at $Q^2 <$ 1.5 GeV$^2$ [4, 17, 18]. The resonant part of the $\pi^+\pi^- p$ electroproduction cross sections are computed by extrapolating the available results to the range of photon virtualities $2.0 < Q^2 < 5.0$ GeV$^2$.

The contributions from resonances in the mass range above 1.8 GeV were not taken into account due the the lack of the experimental results on their electrocouplings, thus limiting our evaluation of these contribution to the range of $W < 1.82$ GeV.

The hadronic decay widths to the $\pi\Delta$ and $\rho p$ final states for the above resonances are taken from previous analyses of the CLAS $\pi^+\pi^- p$ electroproduction data off protons [4, 16–18]. The constraints imposed by the requirement to describe $\pi^+\pi^- p$ electroproduction data with $Q^2$-independent hadronic decay widths of contributing states allows us to obtain improved estimates of the branching fractions (BF) for the resonances listed in Table III.

The resonant contributions to fully integrated $\pi^+\pi^- p$ electroproduction cross sections are shown in Fig. 14 and Fig. 15 at different photon virtualities. They correspond to $W$ ranges that are closest to the central masses of $N(1440)1/2^+$ and $N(1520)3/2^-$ states. The electrocouplings of these low-lying resonances as well as for the $N(1535)1/2^-$ state are available in the entire range of $Q^2$ covered in our measurements [4, 8, 15, 16, 35]. Interpolated values of these electrocouplings are used in the resonant contribution evaluation shown in Figs. 14 and 15. In the mass range from 1.50 GeV to 1.56 GeV there is also a small contribution from the tail of the $\Delta(1620)1/2^-$ resonance. Electrocouplings of this resonance are available at $Q^2 < 1.5$ GeV$^2$ [4]. To evaluate this contribution, the CLAS results were extrapolated into the range $2.0 < Q^2 < 5.0$ $\tilde{\mathrm{G}}$eV$^2$.

The results shown in Figs. 14 and 15 demonstrate a increase with $Q^2$ of the relative resonance contributions to the fully integrated $\pi^+\pi^- p$ electroproduction cross sections. The resonant part begins to dominate at $Q^2 > 4.0$ GeV$^2$.

Table IV shows ratios of projected resonant contributions to the measured cross sections in several $Q^2$-bins averaged within four $W$-intervals that have distinctively different resonant content:

- In the interval $1.41 < W < 1.61$ GeV electrocouplings of the low-lying resonances have been measured in the $Q^2$ range covered here.
- In the mass range $1.61 < W < 1.74$ GeV, several states in the third resonance region contribute, including states that couple preferentially to $N\pi\pi$. Their contribution to the $\pi^+\pi^- p$ cross sections has been evaluated by extrapolating the available electrocouplings from $Q^2 < 1.5$ GeV$^2$ [18] to $2.0 < Q^2 < 5.0$ GeV$^2$.
- The interval $1.74 < W < 1.82$ GeV includes only states recently reported [36], for which no electrocouplings are available to date, and their $N\pi\pi$ couplings are also unknown. Hence no projections are possible in this mass range.

In Figs. 16, 17, 18 we show the comparison of nine one-fold differential $\pi^+\pi^- p$ electroproduction cross sections and the resonant contributions computed in the JM16 model [4, 16, 18] within the given $W$ and $Q^2$ bins.

At $W < 1.74$ GeV, the projected resonance contributions to the measured cross sections are the largest over the entire $Q^2$ range covered here. We find that the relative resonant contributions increase with $Q^2$ and dominate the integrated cross section in the highest $Q^2$-bin centered at 4.6 GeV$^2$.

However, the resonant contributions to the CM-angular distributions at $Q^2 = 4.6$ GeV$^2$ and in the mass range 1.51 GeV to 1.71 GeV shown in Fig. 18 indicate sizeble differences in the angle dependence of the measured differential cross sections and the projected resonance contributions. This suggests substantial contributions from non-resonant mechanisms even at the highest photon virtualities covered by our measurements.

In particular, a comparison of the measured CM-angular distributions for the final $\pi^-$ and the computed

| Exclusive meson electroproduction channels | Nucleon resonances | $Q^2$-ranges for extracted $\gamma_v pN^*$ electrocouplings, GeV$^2$ |
|---|---|---|
| $\pi^0 p$, $\pi^+ n$ | $\Delta(1232)3/2^+$, | 0.16-6.00 |
| | $N(1440)1/2^+$, $N(1520)3/2^-$, $N(1535)1/2^-$ | 0.30-4.16 |
| $\pi^+ n$ | $N(1675)5/2^-$, $N(1680)5/2^+$ | 1.6-4.5 |
| | $N(1710)1/2^+$ | 1.6-4.5 |
| $\eta p$ | $N(1535)1/2^-$ | 0.2-2.9 |
| $\pi^+\pi^- p$ | $N(1440)1/2^+$, $N(1520)3/2^-$ | 0.25-1.5 |
| | $\Delta(1620)1/2^-$, $N(1650)1/2^-$, $N(1680)5/2^+$ | 0.50-1.5 |
| | $\Delta(1700)3/2^-$, $N(1720)3/2^+$, $N'(1720)3/2^+$ | 0.50-1.5 |

TABLE II. Summary of the results on the nucleon resonance electrocouplings available from analyses of the CLAS exclusive meson electroproduction data off protons as of May 2016 [1, 4, 8, 15–17].

| Resonances | $\Gamma_{tot}$, MeV | Branching fraction to the final $\pi\Delta$ states, % | Branching fraction to the final $\rho$ state, % |
|---|---|---|---|
| $N(1440)1/2^+$ | 387 | 19 | 1.7 |
| $N(1520)3/2^-$ | 130 | 25 | 9.4 |
| $N(1535)1/2^-$ | 131 | 2 | 10 |
| $\Delta(1620)1/2^-$ | 158 | 43 | 49 |
| $N(1650)1/2^-$ | 155 | 5 | 6 |
| $N(1680)5/2^+$ | 115 | 21 | 13 |
| $\Delta(1700)3/2^-$ | 276 | 84 | 5 |
| $N(1700)3/2^-$ | 148 | 45 | 52 |
| $N'(1720)3/2^+$ | 115 | 51 | 9 |
| $N(1720)3/2^+$ | 117 | 39 | 44 |

TABLE III. The nucleon resonances included in the evaluation of the resonant contribution to $\pi^+\pi^- p$ electroproduction cross sections off protons, and their total decay widths and branching fractions for decays to the $\pi\Delta$ and $\rho p$ final hadron states used in the evaluation of the resonant contributions to the current measurements.

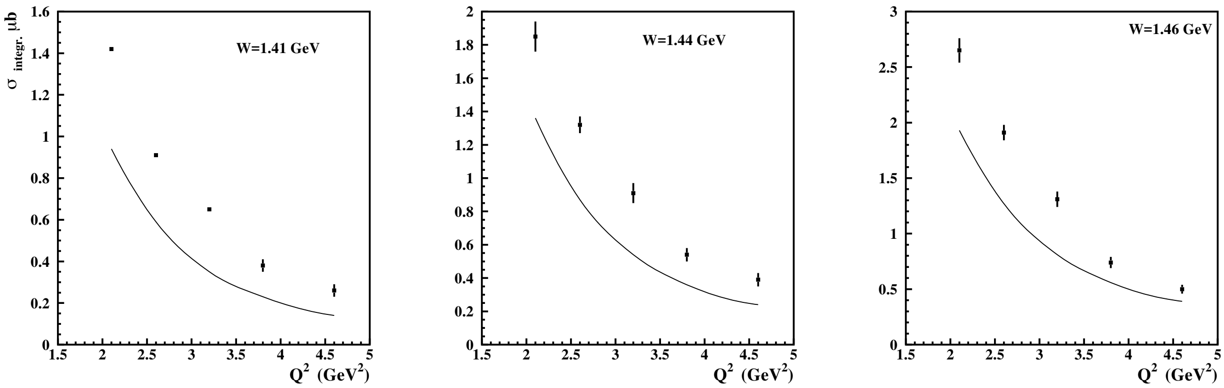


FIG. 14. The resonant contributions computed as described in Section III (solid lines) in comparison with the CLAS results on fully integrated $\pi^+\pi^- p$ electroproduction cross sections off protons (points with error bars) in three $W$-bins near the central mass of $N(1440)1/2^+$ state: $W$=1.41 GeV (left), $W$=1.44 GeV (center), $W$=1.46 GeV (right)

| $Q^2$, GeV$^2$ | $1.41 < W < 1.61$, GeV | $1.61 < W < 1.74$, GeV | $1.74 < W < 1.82$, GeV |
|---|---|---|---|
| 2.1 | 0.65 ± 0.033 | 0.57 ± 0.034 | 0.20 ± 0.019 |
| 2.6 | 0.57 ± 0.029 | 0.50 ± 0.028 | 0.18 ± 0.010 |
| 3.2 | 0.55 ± 0.029 | 0.49 ± 0.029 | 0.19 ± 0.017 |
| 3.8 | 0.66 ± 0.034 | 0.62 ± 0.034 | 0.21 ± 0.014 |
| 4.6 | 0.75 ± 0.041 | 0.79 ± 0.049 | 0.24 ± 0.017 |

TABLE IV. Ratios of resonant contributions computed within the framework of the current JM model version [4, 16, 18] over measured fully integrated $ep \rightarrow e'\pi^+\pi^- p$ cross sections averaged within three $W$-intervals with different resonant content

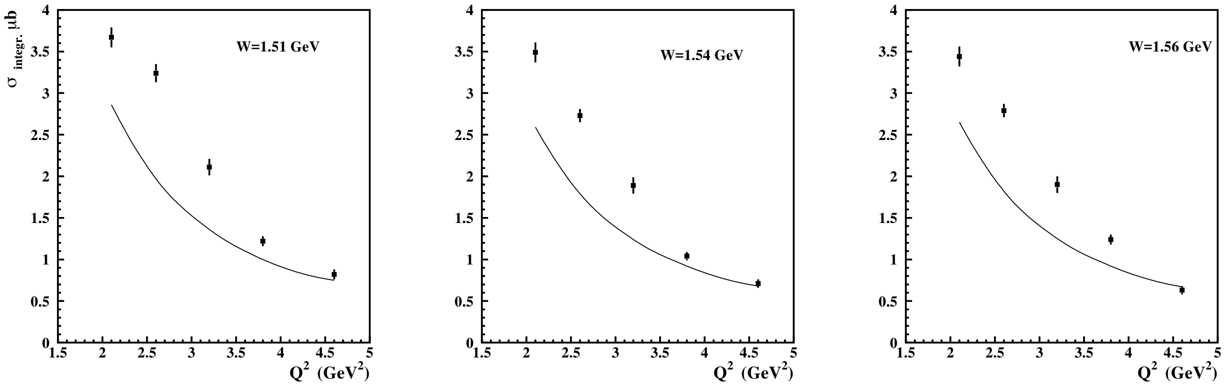


FIG. 15. The resonant contributions computed as described in Section III (solid lines) in comparison with the CLAS results on fully integrated $\pi^+\pi^-p$ electroproduction cross sections off protons (points with error bars) in three $W$-bins near the central mass of $N(1520)3/2^-$ state: $W$=1.51 GeV (left), $W$=1.54 GeV (center), $W$=1.56 GeV (right)

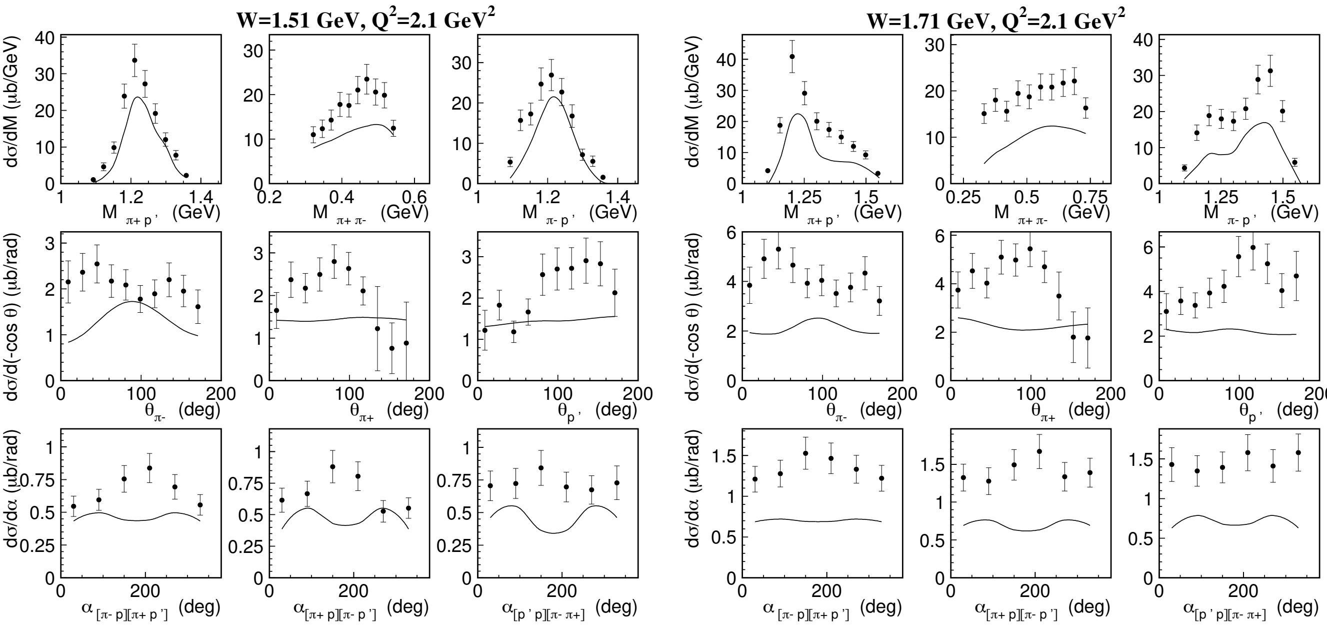


FIG. 16. The resonant contributions (solid lines) to nine one-fold differential $\pi^+\pi^-p$ electroproduction cross sections in the representative $W$-bins inside two $W$-intervals of distinctively different resonant content described in Section III at $Q^2$=2.1 GeV$^2$.

resonant contributions shown in Fig. 18 suggests that the non-resonant contribution from the $\pi^-\Delta^{++}$ intermediate state created in the t-channel exchange dominates at forward angles. Also, the presence of a direct $2\pi$ production mechanisms may explain the differences between the measured cross sections and the resonant contributions seen at the backward $\pi^-$ angles.

In the $W$-interval from 1.74 GeV to 1.82 GeV the ratio of projected resonant contributions to the fully integrated $\pi^+\pi^-p$ electroproduction cross sections decreases by more than the factor two in all $Q^2$-bins covered here (Table IV). In order to achieve a satisfactory description of the data in this mass range, with resonant contributions from the aforementioned resonances only, requires an increase of the relative contribution from non-resonant mechanisms by more than a factor of two, which seems unlikely.

The data discussed here therefore present the opportunity to independently verify signals from new baryon states reported in the Bonn-Gatchina photoproduction data analysis [21]. A successful description of the $\pi^+\pi^-p$ photo- and electro-production data with $Q^2$-independent

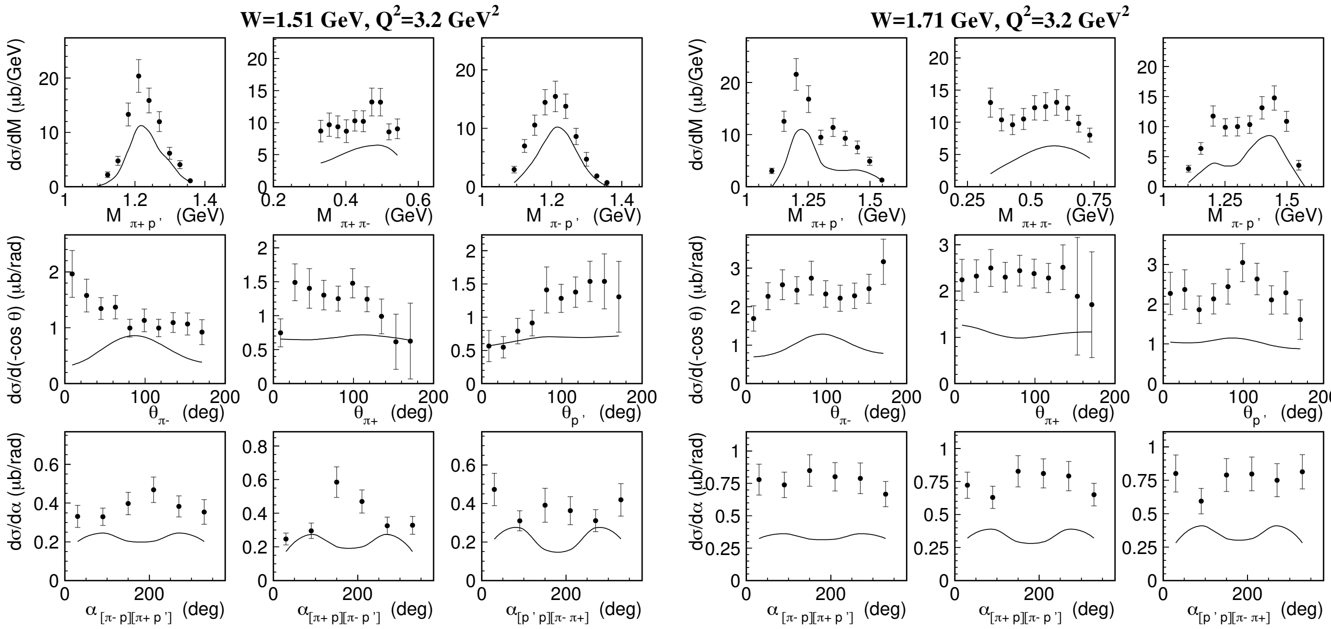


FIG. 17. The resonant contributions (solid lines) to nine one-fold differential $\pi^+\pi^-p$ electroproduction cross sections in the representative $W$-bins inside two $W$-intervals of distinctively different resonant content described in Section III at $Q^2$=3.2 GeV$^2$.

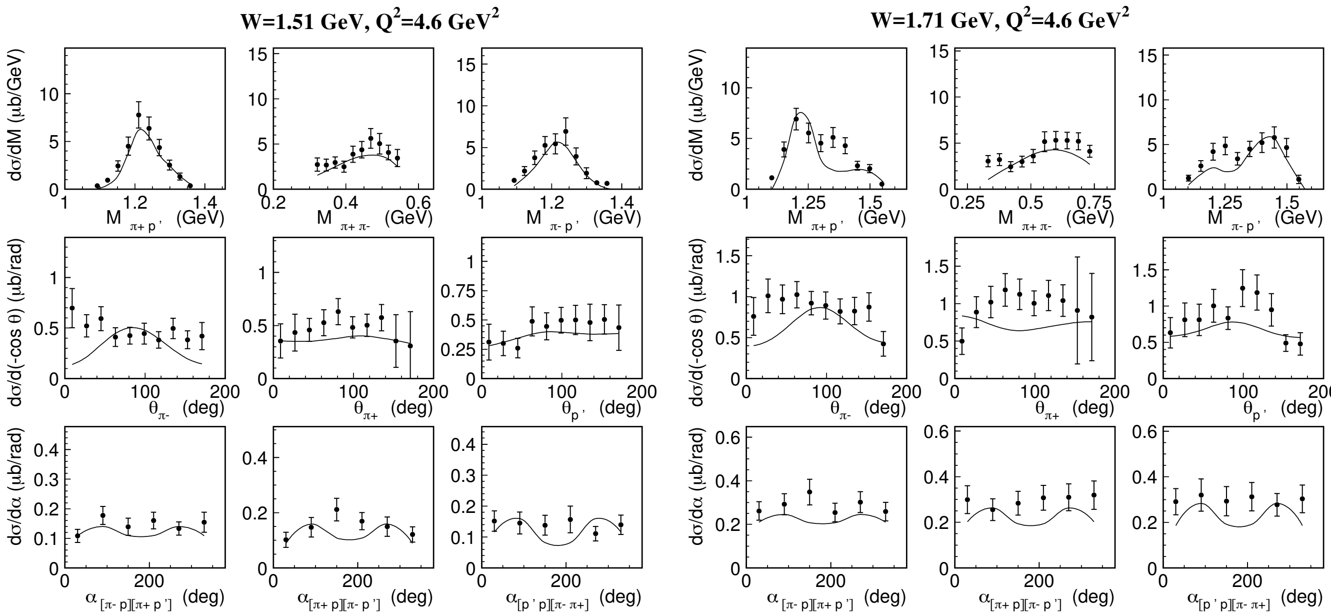


FIG. 18. The resonant contributions (solid lines) to nine one-fold differential $\pi^+\pi^-p$ electroproduction cross sections in the representative $W$-bins inside two $W$-intervals of distinctively different resonant content described in Section III at $Q^2$=4.6 GeV$^2$.

resonance parameters (such as partial $\pi\Delta$ and $\rho p$ decay widths) would provide model independent evidence of these newly claimed excited states.

According to Table IV, at $W < 1.74$ GeV the relative resonant contributions decrease in the $Q^2$ range from 2.0 GeV$^2$ to 3.0 GeV$^2$, while at $Q^2 > 3.0$ GeV$^2$ the relative resonant contributions exhibit an increase with $Q^2$. For resonances in the mass range from 1.41 GeV to 1.61 GeV, the electrocouplings are known from CLAS data in the entire range of photon virtualities covered by our measurements. Therefore, this effect can not be related to uncertainties resulting from the extrapolations of resonance electrocouplings..

Our data suggest that at $Q^2 < 3.0$ GeV$^2$ the resonance contributions decrease with $Q^2$ faster in comparison with other contributing mechanisms. Instead, at $Q^2 > 3.0$ GeV$^2$ resonance contributions decrease with $Q^2$ slower in comparison with the remaining contributions to exclusive $\pi^+\pi^-p$ electroproduction. Such behavior supports the assessment of the structure of the $N^*$ states from analyses of exclusive meson electroproduction [1, 4] as an interplay of the inner core of three dressed quarks and the external meson-baryon cloud. The range of $Q^2 < 3.0$ GeV$^2$ correspond to substantial contributions from the meson-baryon cloud which becomes largest at the photon point. This contribution decreases with $Q^2$ faster than the contribution from non-resonant mechanisms and its relative resonant contribution decreases with $Q^2$ at $Q^2 < 3.0$ GeV$^2$. Instead, at higher $Q^2$ the contribution from the quark core becomes more significant, even dominant, and this contribution decreases with $Q^2$ slower than non-resonant processes causing relative growth of the resonant cross sections.

## IV. CONCLUSION

In this paper we presented new electroproduction data on $ep \to ep\pi^+\pi^-$ in the mass range $W < 2.0$ GeV, and at photon virtualities $2.0 < Q^2 < 5$ GeV$^2$. The kinematics covered is rich with known nucleon resonances whose electrocouplings are either unknown or known from N$\pi$ electroproduction only. In particular, these data covers the range of $W > 1.6$ GeV, where many resonances couple predominantly to the $N\pi\pi$ final state, and hence can be studied here.

The extraction of the electrocoupling amplitudes requires a reaction model that must include all well established resonances in amplitude form, along with the amplitudes of the relevant non-resonant mechanisms and the interference of the contributing amplitudes. One such model is the JM framework [4, 16, 18], but its reach in the invariant mass of the final hadrons $W$ and photon virtuality $Q^2$ must be extended into the kinematic domains of the new data. This effort is underway and the results will be part of a future paper on the subject.

The projected resonant contributions to the cross sections discussed in section III were obtained within the framework of the unitarized Breit-Wigner ansatz of the JM model [16]. The resonant cross sections were evaluated with electrocouplings determined by interpolations and extrapolations of the available results on these resonance parameters [33, 34] from the measured $Q^2$ into new territory.

With this said, we see strong indications that the relative contribution from the resonant cross sections at $W < 1.74$ GeV increases with $Q^2$. It suggest good prospects for exploration of the electrocouplings of the nucleon resonances in this mass range and with photon virtualities up to 5.0 GeV$^2$ and above. With the CEBAF accelerator upgrade to an energy of 12 GeV, employing the new CLAS12 detector, photon virtualities in the range $5.0 < Q^2 < 12.0$ GeV$^2$ can be reached for all of the prominent resonances with masses below 2.0 GeV. The range of $Q^2 > 2.0$ GeV$^2$ is of particular importance to study the momentum dependence of the light-quark masses, as the $Q^2$ dependence of the resonance electrocouplings is sensitive to the quark mass function [12, 13].

The data presented here provides a basis to verify the existence of possible new baryon states reported at $M > 1.8$ GeV in a global multichannel partial wave analysis by the Bonn-Gatchina group [24]. The apparent increase in the sensitivity of resonant contributions with increasing $Q^2$, as shown in Table IV, suggests that more resonances in this mass range will be needed to describe the present data, as well as the possibility to locate new baryon states by examining how to describe these data with $Q^2$ independent hadronic parameters for the excited nucleon states.

This provides a sensitive means of testing computations of the electrocouplings from first principles QCD as incorporated in DSE approach [10, 11]. In addition, reaching higher mass states at 2 GeV and above will allow testing of quark model prediction employing light-front dynamics [5] and other approaches [37] in a domain where first principles calculations are still unavailable.

## ACKNOWLEDGMENTS

We are expressing our gratitude for the efforts of the staff of the Accelerator and Physics Divisions at Jefferson Lab that made this experiment possible. This work was supported in part by the U.S. Department of Energy (DOE) and National Science Foundation (NSF), the Skobeltsyn Institute of Nuclear Physics (SINP) and the Ohio University (OU). The Jefferson Science Associates (JSA) operates the Thomas Jefferson National Accelerator Facility for the United States Department of Energy under contract DE-AC05-06OR23177.

[1] I. G. Aznauryan and V. D. Burkert, Prog. Part. Nucl. Phys. **67**, 1 (2012).

[2] I. G. Aznauryan *et al.*, Int. J. Mod. Phys. E **22**, 1330015 (2013).

[3] I. G. Aznauryan, V. D. Burkert, and V. I. Mokeev, ArXiv e-prints (2015), arXiv:1509.08523 [nucl-ex].

[4] V. I. Mokeev *et al.*, Phys. Rev. C **93**, 025206 (2016).

[5] I. G. Aznauryan and V. D. Burkert, Phys. Rev. C **92**, 015203 (2015).

[6] N. Suzuki, T. Sato, and T.-S. H. Lee, Phys. Rev. C **82**, 045206 (2010).

[7] V. M. Braun *et al.*, Phys. Rev. D **89**, 094511 (2014).

[8] I. G. Aznauryan *et al.* (CLAS Collaboration), Phys. Rev. C **80**, 055203 (2009).

[9] I. V. Anikin, V. M. Braun, and N. Offen, Phys. Rev. D **92**, 014018 (2015).

[10] J. Segovia *et al.*, Few-Body Systems **55**, 1185 (2014).

[11] J. Segovia *et al.*, Phys. Rev. Lett. **115**, 171801 (2015).

[12] C. D. Roberts, J. Phys. Conf. Ser. **706**, 022003 (2016).

[13] C. D. Roberts, in *Proceedings of the 10th International Workshop on the Physics of Excited Nucleons (NSTAR2015)* (2016) p. 010012, arXiv:1509.08952 [nucl-th].

[14] I. C. Cloët and C. D. Roberts, Prog. Part. Nucl. Phys. **77**, 1 (2014).

[15] K. Park *et al.* (CLAS Collaboration), Phys. Rev. C **91**, 045203 (2015).

[16] V. I. Mokeev *et al.* (CLAS Collaboration), Phys. Rev. C **86**, 035203 (2012).

[17] V. I. Mokeev and I. G. Aznauryan, J. of Phys. Conf. Ser. **26**, 1460080 (2014).

[18] Mokeev, V. I. *et al.*, EPJ Web Conf. **113**, 01013 (2016).

[19] V. I. Mokeev, Few-Body Systems **57**, 909 (2016).

[20] M. Ripani *et al.* (CLAS Collaboration), Phys. Rev. Lett. **91**, 022002 (2003).

[21] A. V. Anisovich *et al.*, Eur. Phys. J. A **48**, 15 (2012).

[22] G. V. Fedotov *et al.* (CLAS Collaboration), Phys. Rev. C **79**, 015204 (2009).

[23] V. I. Mokeev *et al.*, Phys. Rev. C **80**, 045212 (2009).

[24] A. V. Anisovich *et al.*, Eur. Phys. J. A **50**, 129 (2014).

[25] H. Kamano *et al.*, Phys. Rev. C **88**, 035209 (2013).

[26] H. Kamano *et al.*, Phys. Rev. C **94**, 015201 (2016).

[27] B. Mecking *et al.*, Nucl. Instr. and Meth. **503**, 513 (2003).

[28] L. W. Mo and Y. S. Tsai, Rev. Mod. Phys. **41**, 205 (1969).

[29] I. G. Aznauryan *et al.*, Phys. Rev. C **72**, 045201 (2005).

[30] V. I. Mokeev *et al.*, Phys. Atom. Nucl. **64**, 1292 (2001).

[31] M. Ripani *et al.*, Nucl. Phys. A **672**, 220 (2000).

[32] P. E. Bosted, Phys. Rev. C **51**, 409 (1995).

[33] G. V. Fedotov, `https://userweb.jlab.org/~mokeev/resonance/electrocouplings/`.

[34] E. L. Isupov, See Supplemental Material at [URL will be inserted by publisher] (2017).

[35] H. Denizli *et al.* (CLAS Collaboration), Phys. Rev. C **76**, 015204 (2007).

[36] Particle Data Group, K. A. Olive *et al.*, Chinese Physics C **38**, 090001 (2014).

[37] E. Santopinto and M. M. Giannini, Chin. J. Phys. **53**, 020301 (2015).